MANCHESTER 1824
The University of Manchester

The University of Manchester Research

Characterising the loading direction sensitivity of 3D woven composites: Effect of z-binder architecture

DOI:
10.1016/j.compositesa.2016.08.028

Document Version
Accepted author manuscript

Link to publication record in Manchester Research Explorer

Citation for published version (APA):
Saleh, M., Yudhanto, A., Potluri, P., Lubineau, G., & Soutis, C. (2016). Characterising the loading direction sensitivity of 3D woven composites: Effect of z-binder architecture. *Composites Part A: Applied Science and Manufacturing*, *90*, 577-588. https://doi.org/10.1016/j.compositesa.2016.08.028

Published in:
Composites Part A: Applied Science and Manufacturing

Citing this paper
Please note that where the full-text provided on Manchester Research Explorer is the Author Accepted Manuscript or Proof version this may differ from the final Published version. If citing, it is advised that you check and use the publisher's definitive version.

General rights
Copyright and moral rights for the publications made accessible in the Research Explorer are retained by the authors and/or other copyright owners and it is a condition of accessing publications that users recognise and abide by the legal requirements associated with these rights.

Takedown policy
If you believe that this document breaches copyright please refer to the University of Manchester's Takedown Procedures [http://man.ac.uk/04Y6Bo] or contact uml.scholarlycommunications@manchester.ac.uk providing relevant details, so we can investigate your claim.

OPEN ACCESS

Download date:30. Jun. 2022

Accepted Manuscript

Characterising the loading direction sensitivity of 3D woven composites: Effect of z-binder architecture

Mohamed Nasr Saleh, Arief Yudhanto, Prasad Potluri, Gilles Lubineau, Constantinos Soutis

PII: S1359-835X(16)30284-6
DOI: http://dx.doi.org/10.1016/j.compositesa.2016.08.028
Reference: JCOMA 4404

To appear in: *Composites: Part A*

Received Date: 24 December 2015
Revised Date: 28 May 2016
Accepted Date: 23 August 2016

Please cite this article as: Saleh, M.N., Yudhanto, A., Potluri, P., Lubineau, G., Soutis, C., Characterising the loading direction sensitivity of 3D woven composites: Effect of z-binder architecture, *Composites: Part A* (2016), doi: http://dx.doi.org/10.1016/j.compositesa.2016.08.028

This is a PDF file of an unedited manuscript that has been accepted for publication. As a service to our customers we are providing this early version of the manuscript. The manuscript will undergo copyediting, typesetting, and review of the resulting proof before it is published in its final form. Please note that during the production process errors may be discovered which could affect the content, and all legal disclaimers that apply to the journal pertain.

ACCEPTED MANUSCRIPT

Characterising the loading direction sensitivity of 3D woven composites: effect of z-binder architecture

Mohamed Nasr Saleh[1], Arief Yudhanto[2], Prasad Potluri[1], Gilles Lubineau[2], Constantinos Soutis[3]

[1]School of Materials, University of Manchester, Manchester, M13 9PL, UK

[2]King Abdullah University of Science and Technology (KAUST), Physical Sciences and Engineering Division, COHMAS Laboratory, Thuwal 23955-6900, Saudi Arabia

[3]Aerospace Research Institute, University of Manchester, M1 3NJ, UK.

Abstract

Three different architectures of 3D carbon fibre woven composites (orthogonal, ORT; layer-to-layer, LTL; angle interlock, AI) were tested in quasi-static uniaxial tension. Mechanical tests (tensile in on-axis of warp and weft directions as well as 45° off-axis) were carried out with the aim to study the loading direction sensitivity of these 3D woven composites. The z-binder architecture (the through-thickness reinforcement) has an effect on void content, directional fibre volume fraction, mechanical properties (on-axis and off-axis), failure mechanisms, energy absorption and fibre rotation angle in off-axis tested specimens. Out of all the examined architectures, 3D orthogonal woven composites (ORT) demonstrated a superior behaviour, especially when they were tested in 45° off-axis direction, indicated by high strain to failure (~23%) and high translaminar energy absorption (~40 MJ/m^3). The z-binder yarns in ORT architecture suppress the localised damage and allow larger fibre rotation during the fibre "scissoring motion" that enables further strain to be sustained by the in-plane fabric layers during off-axis loading.

Keywords: A. Carbon fibre, A. 3-Dimensional reinforcement, C. Damage mechanics, D. Mechanical testing

ACCEPTED MANUSCRIPT

1 Introduction

Two-dimensional (2D) laminated composites, offering high in-plane stiffness and strength, have been widely used to build structures in automotive and aerospace industries. However, 2D composites are generally weak in the thickness direction (z-axis). Some applications of composites, nonetheless, require excellent out-of-plane properties for delamination resistance and impact damage resistance, e.g., wind turbine blades, airframe stringers and stiffeners and pressure vessels. Three-dimensional (3D) composites are thus an excellent choice for such applications. One class of 3D composites that receives a great attention is 3D woven composites whereby longitudinal yarns ("warp" or 0° fibre tows), transverse yarns ("weft" or 90° fibre tows) and through-thickness yarns (z-binder) are interlaced with a specific weaving architecture. 3D woven composite architectures can be grouped (according to the angle between the binding yarns and the in-plane yarns "warp/weft") into two main groups. When the interlacement angle is 90^{o}, the 3D woven composite is called Orthogonal; other than that, it is referred to as Angle Interlock. Then, these two main groups can be further subdivided into layer to layer (binder goes between layers) or through-thickness (binder goes through the entire thickness). This interlacing process to produce 3D woven fabric can be done at faster rates since the existing textile technology can be adopted. As such, design flexibility to produce various weaving architecture is achieved, and near-net-shape preforms can be attained [1]. The delamination resistance [1] and impact performance [2–6] of 3D woven composites have been found to be outstanding thanks to the effectiveness of through-thickness reinforcement yarn (z-binder) in resisting "preventing" the growth of damage (delamination between plies).

Although the potential use of 3D woven composites is clearly apparent, their application is still limited [7] for various reasons. The first reason is that 3D woven composites generally exhibit lower in-plane properties in comparison with 2D non-crimp fabric (NCF) laminated composites [8,9] since they are inherently characterised by undulation or "crimp". This crimp is a direct result of the interlacement of longitudinal, transverse and through-thickness yarns [10]. The degree of crimp is dependent on the adopted woven architectures and the tension force during the weaving process. Secondly, the damage mechanisms in 3D woven composites are complex as they involve interaction

ACCEPTED MANUSCRIPT

among damage modes within and between yarns, effect of rich resin regions, voids and geometrical imperfections due to the manufacturing and compaction process. Thirdly, 3D woven composites are loading sensitive as yarns are distributed in three directions. For instance, the response of 3D woven composites in warp and weft directions can be different. The problem is more complex when off-axis (bias) loading is considered. Nevertheless, complex shape of composite structures, e.g., turbine blade structure, may be subjected to various degree of off-axis loading even when the structure itself is uniaxially loaded. In light of potential use of 3D woven composites for such impact-prone structures, it is thus important to understand the behaviour of various types of 3D woven composites under different loading directions. One of the assessments is through simple tensile tests on various 3D woven architectures under on-axis (warp- and weft-directions) and off-axis loadings (bias direction). Such assessment is also essential to evaluate the efficacy of "energy-based" design where the energy absorbed by 3D woven composite is considered. As such, the underlying mechanism behind the absorbed energy in various types of 3D woven composites under in-plane loading directions can be understood.

Much work has been done to characterise the failure mechanisms of 3D woven composites under tension [6,11–22] along the warp- or weft-directions. Gerlach *et al.* [6] who investigated angle interlock 3D woven composites subjected to tension (warp, weft) showed that the effect of z-binder volume fraction on the in-plane properties is minor. Cox *et al*. [14,15] studied the failure mechanism of 3D woven composites (orthogonal, layer-to-layer) monotonically loaded in tension, compression and bending. They found that the dominant failure modes in 3D interlock woven composites are tow rupture and pull-out (tension case), delamination and kink-band formation (compression case), combination of those failure modes (bending case). Influence of fabric architecture in 3D woven composite under tensile, compressive and bending loads was investigated by Dai *et al.* [11] where they found that the mechanical performance is affected by resin rich region and waviness of load-carrying fibres. They also showed that angle interlock outperforms orthogonal 3D woven composite for all loading conditions. For 3D orthogonal woven composites under tension, Lomov *et al.* [16] found that damage initiates firstly at binder interlacement points. It is then followed by transverse cracks in yarns perpendicular to the loading direction and

ACCEPTED MANUSCRIPT

local delamination between yarns. Final failure is characterised by fibre failure that leads to complete rupture of specimen. Warren, *et al.* [21] characterised the global stress-strain curves and failure modes of 3D twill harness orthogonal woven composite, 3D layer-to-layer woven composite and 2D woven architecture under warp and weft tensions. In-plane shear test was also carried out using V-notched rail shear method, where they found that the shear among adjacent tows and matrix degradation are the dominant damage mechanisms in shear. Visrolia and Meo [22] performed on-axis tension (0° direction), off-axis tension (45° direction) and compression tests to validate their modelling strategy for 3D orthogonal woven composite. A good agreement of global stress-strain was demonstrated between their proposed model and the experimental results, although for off-axis tension the experimental results were reported up to 3% strain only (not until failure) and the damage mechanism under shear was not revealed. Pochiraju and Chou [19] reported the behaviour of 3D woven composites (layer-to-layer angle interlock, through-thickness angle interlock) under tension in warp and weft directions. Nonetheless, limited work has been performed to characterise 3D woven composites under off-axis loading (bias direction). Off-axis loading studies have been reported for non-crimp fabric (NCF) composites [23]. Ivanov *et al*. [24] have reported loading direction sensitivity (warp, weft, bias) of 3D woven composites but the materials were limited to orthogonal architecture. Nevertheless, there is still a need to evaluate the loading sensitivity of various architectures of 3D woven composites subjected to warp, weft and bias loadings. The relationship between damage mechanisms and energy absorption also needs to be revealed.

This research work aims to extend the characterisation of 3D woven composites with the main focus on the off-axis tensile loading (bias 45^{o}). Three types of 3D woven architecture are considered here: (i) layer-to-layer (LTL), (ii) angle interlock (AI), and (iii) orthogonal (ORT). The materials were loaded, in tension, in warp, weft and bias (45°) directions where global stress-strain curves, failure mechanisms and energy absorption were assessed. This paper is divided into five sections. Section 2 describes the architecture of 3D woven composites used in present experiments, and their manufacturing details. Section 3 describes the material characterisation (fibre volume fraction measurement) and mechanical tests (tensile tests coupled with digital image correlation analysis). Section 4

ACCEPTED MANUSCRIPT

presents the results and discusses the experimental findings (effect of z-binder on directional volume fraction, stress-strain responses, failure mechanism and energy absorption). Finally, section 5 highlights the concluding remarks of the paper.

2 Materials and manufacturing

The carbon fibre, used in this study, is HexTow IM7 (Hexcel), while the epoxy is MTM 57 (medium temperature epoxy produced by Cytec). The 3D woven dry fabrics are produced by Sigmatex UK. Three architectures are investigated, namely orthogonal (ORT), layer-to-layer (LTL) and angle interlock (AI). Fig. 1 shows the schematic architecture of three 3D woven fabrics drawn using TexGen software. Specification of the textile architecture parameters of 3D woven composites are detailed in Table 1. Warp and weft fibre count for ORT, AI and LTL is 12k. The z-binder fibre count for ORT, AI and LTL is 6k, 6k and 12k, respectively. The number of warp threads, weft threads and z-binder threads per unit length (centimetre) is specified in Table 1 as ends/cm, picks/cm and binders/cm, respectively. In addition, the areal density of the dry 3D woven fabric is also given in Table 1 (unit is g/m^2).

To produce 3D woven composite panels, the dry fabrics were infiltrated by MTM 57 epoxy matrix using resin film infusion (RFI) process. Infusion process was carried out at 70°C for 1 h, while curing process was done at 120°C for 1 h. Minimum curing pressure for MTM 57 was set to 2.8 bars. Once the 3D woven composite panels with the size of 300 mm x 200 mm were cured, they were cut into three different orientations (see Fig. 2). Thickness of cured composite panels ranges between 3.2 to 3.6 mm depending on the warp and weft number of layers.

3 Experimental procedures

3.1 X-ray computed tomography

In order to evaluate the deviation, of the "as-manufactured" 3D woven composite panels, from the idealised geometry and compare afterwards with the damaged specimens, X-ray CT scans were performed on the three architectures (ORT, LTL and AI) using a Zeiss Xradia VersaXRM-510 machine. To obtain a sufficient resolution, a square cross

ACCEPTED MANUSCRIPT

section of (30 mm x 30 mm) was cut from the sample. The 0.4x objective of the scanner was used. For ORT sample, the total volume in the field of view was 10 x 10 x 10 mm^3, resulting in a voxel size of 5 μm. The source voltage and current were set to 40 kV and 75 μA respectively. The exposure time for each radiograph was 10 s, with 1600 radiographs being collected over 360o. The total data acquisition time was 7 hours. Similarly, all scanning parameters were kept the same for LTL and AI except for the total volume in the field of view and consequently the voxel size. As both LTL and AI have larger unit cells, the field of view was increased to 16 x 16 x 16 mm^3 and 25 x 25 x 25 mm^3 respectively.

After scanning, the 3D unit cells (Fig. 3a, c, e) were reconstructed out of the 2D X-ray slices for ORT, LTL and AI. Using a cutting plane parallel to the warp yarns, X-CT section view (Fig. 3b, d, f) clearly shows voids and binder distortion, due to weaving process, RFI process and fabric compaction for all the architectures that can have impact on stiffness, damage initiation and ultimate specimen failure. In addition, in the case of LTL architecture (Fig. 3d), the weft layers are distorted in the vertical plane and resin rich regions are shown in black. Unlike ORT and LTL architectures, the AI architecture cross section (Fig. 3f) suggests that it has the most severe binder distortion.

3.2 Determination of fibre volume fraction

In this study, the determination of fibre volume fraction of the manufactured panels was conducted in two stages. The first stage deals with an experimental measurement of fibre volume fraction V_f (as well as matrix V_m and void volume fraction V_v) of samples from the manufactured panels. The second stage deals with an analytical calculation to determine directional V_f in warp, weft and z-directions based on textile parameters given in Table 1. The procedures of both stages are described in the following sections.

3.2.1 Acid digestion

Fibre volume fraction measurement was conducted based on acid digestion technique according to ASTM D3171 standard (Constituent Content of Composite Materials). The procedure is generally described as follows: (i) specimen is immersed in the sulfuric acid where the matrix is entirely dissolved; (ii) weight of the specimen is measured before and after the digestion process. The measurement of fibre volume fraction by acid digestion also enables the measurement of the matrix volume fraction as well as void

ACCEPTED MANUSCRIPT

content. Readers are referred to the ASTM D3171 document for more detailed experimental and specimen requirements.

3.2.2 Directional fibre volume fraction analysis

Directional fibre volume fraction analysis aims to calculate fibre volume fraction in warp, weft and z-directions, and to eventually determine the contribution of each directional fibre tows on the overall V_f. The calculation of directional V_f can be summarised as follows: first, directional areal density of the fabric in warp, weft and z-binder direction is calculated by multiplying the yarns' count (in tex) by ends/cm, picks/cm and binders/cm, respectively. Second, the directional areal density is then normalised by the total areal density to determine the percentage of warp, weft and z-binder fibres (directional V_f).

3.3 Tensile testing

Tensile test was carried out on on-axis (warp, weft) and 45° off-axis specimens of LTL, AI and ORT. Instron 5882 with 100 kN load cell was used to apply a displacement-controlled tension with loading speed of 2 mm/min according to ASTM D3039 standard (Tensile Properties of Polymer Matrix Composite Materials). Four specimens were tested for each type (LTL, AI, and ORT) and each orientation (0^o, 90^o and 45^o). Specimens' dimensions were in accordance with ASTM D3039 standard, i.e. 250 mm long and 25 mm wide with a gauge length of 150 mm. All tests were performed in a controlled environment where the temperature was 21^oC and the relative humidity (RH) was 45%. The tensile test setup shown in Fig. 4a consists of two main data acquisition channels for load and displacement within Instron 5882. Strains were acquired using digital image correlation (DIC) system utilising SensiCam 12-bit CCD camera (PCO) with TC-2336 bi-telecentric lenses (The Telecentric Company) shown in Fig. 4a. The resolution of CCD camera was 1376x1040 pixels. The bi-telecentric lenses has a depth of field of 11 mm, diameter of 61 mm and magnification of 0.234 x. Fig. 4b shows a typical speckle pattern on a specimen's surface. CamWare V3.11 software was used to capture the speckle pattern images acquired from the CCD camera. Similar setting has been successfully used for 3D stitched composites, and proven to provide reasonable quality of strain fields for 3D composites [25]. The frame rate is set as 0.5 and 0.33 frames per second (fps) for on-axis and off-axis tensile testing, respectively. The main reason for the lower fps in off-axis tests is that the

ACCEPTED MANUSCRIPT

deformation up to failure in off-axis specimens is much larger than that in on-axis tests. The speckle images were then processed using Vic 2D. In processing these images, the subset size was set to the maximum value of 101 x 101 pixels adequate for woven specimens. In addition, the step size (distance between subsets) was set to 5 pixels. The observation window of approximately 25 x 22 mm^2 produced an image with dimensions of 1040x896 pixels. Global mean values of strains ($\varepsilon_{xx};\varepsilon_{yy};\varepsilon_{xy}$) are obtained from DIC analysis using Vic 2D.

4 Results and discussion

4.1 Effect of z-binder on directional V_f

Table 2 shows the fibre, matrix and void volume fractions of 3D woven composites. LTL exhibits higher V_f of 59.16% in comparison to other materials due to its higher amount of z-binder (12k). However, it is noteworthy that z-binders generally introduces higher amount of void in 3D woven composites in comparison to 2D composites [7,8]. The architecture of z-binder reduces the amount of resin that is flowing into areas between warp and weft tows. This is also aggravated by the fact that RFI process does not employ a transportation medium for resin to flow. In other words, Table 2 suggests that weaving architecture affects the void content "porosity" of the infused panel. AI architecture has a smoother weaving pattern as compared to ORT, while the LTL architecture has the smoothest weaving pattern among all 3D woven investigated architectures. Smoother weaving pattern improves the resin flow between fabric layers and resin infiltration into the fabrics. As such, smoother weaving pattern would have lower void content. This explains the lower void content in the LTL materials. As also observed, the void content in AI is greater than the LTL, but less than that in ORT, which has the most complex weaving pattern and consequently the highest void content. The total fibre volume fraction given in Table 2 is then divided into warp, weft and z-binder content, and Table 3 shows the so-called directional V_f.

4.2 Effect of z-binder on on-axis mechanical properties

The stress-strain curves for ORT, LTL and AI tested up to failure are shown in Fig. 5a-c, respectively. The stress-strain curves, either in warp or weft direction, demonstrate

ACCEPTED MANUSCRIPT

good repeatability. The curves for ORT and LTL shown in Figs. 5a and b indicate that the specimens tested in weft direction are stiffer and stronger that those tested in warp direction. This is primarily due to the fact that ORT and LTL specimens have higher directional V_f in weft direction than that in warp direction (see Table 3). When directional V_f is similar between weft and warp directions, as in the case of AI specimens, the tensile stress-strain curves exhibit similar trend (Fig. 5c). Based on the stress-strain curves shown in Figs. 5a-c, the mechanical properties (Young's modulus, tensile strength and failure strain) of 3D woven composites are given in Table 4.

The strain contour (ε_{yy}) obtained by the DIC system from the surface of ORT, LTL and AI specimens captured at ultimate stress is plotted in Figs. 6a-c. A spectrum of colour map on the right side of each DIC image corresponds to the strain values. The region with high strain values is indicated with red colour, and this region is the interlacement points between z-binders and weft yarns. In addition, the strain contour obtained by DIC was also used to identify the unit cell of 3D woven composites based on the periodicity of the weaving pattern. Here, the dimension of the unit cell of ORT, LTL and AI specimens are identified to be approximately 5 x 5 mm^2, 10 x 7 mm^2 and 20 x 25 mm^2, respectively. The periodicity of the strain contours could be useful for validating the models of 3D woven composites utilising, for instance, asymptotic expansion homogenisation method reported in [22,26–28] and the full-field measurement-based identification models [29].

4.3 Effect of z-binder on off-axis mechanical properties

Stress-strain curves of 3D composites loaded in bias direction of 45° are shown in Fig. 7 where they show bilinear response. The "knee point" is defined as the transition point from the first to the second linear curve; and similar to angle ply laminate case reported in [30] this second linear curve is associated with matrix cracking and inter-yarn matrix delamination that leads to gradual change of stiffness. As shown in Fig. 8, the failure strain of ORT, LTL and AI is 24.20%, 11.27% and 13.29% respectively. The z-binders affect the rotation of biased fibre tows, and eventually the strain hardening and failure onset of 3D woven composites. Table 5 summarises the tensile modulus, strength and failure strain which are derived from the off-axis stress-strain curves. Both AI and ORT demonstrate higher strength and strain to failure compared to LTL which suggests that

ACCEPTED MANUSCRIPT

through-thickness binder improves the performance of off-axis loaded 3D woven composites compared to the layer-to-layer binder. Moreover, the effect of the z-binder yarns architecture is obvious when ORT is compared against AI. The following sections investigate in detail the effect of the z-binder architecture on the off-axis 3D woven composites' strength, damage mechanisms and energy absorption.

Remarks:

1- For LTL and AI a necking region is developed that leads to final fracture. Before localisation, the measured strain is considered as a good estimation of the developed strain. However If localisation occurs outside the ROI of the DIC, the strain measured might not be accurate. The dashed line on Fig. 7 indicates the value after which the strain measurement might not be valid.

2- Approaching the point of failure in off-axis samples, several fibre bundles ruptured from the specimen surface within the DIC region, which caused some of the speckle pattern to debond. This might have an effect on determining the ultimate failure strain which is reported in Table 5. In this study, for the determination of failure strain, it was decided to select the point at which the strain value has not yet being disturbed. Unfortunately, conventional strain gauges bonded on the specimen or non-contact strain gauges would suffer from the same problem.

4.4 Effect of z-binder on failure mechanism

Macroscopic failure of 3D woven composites tested on-axis is shown in Fig. 8. The failure is characterised by a clear transverse fracture (perpendicular to the loading direction) across the whole width of the specimens. This indicates that the final fracture is predominantly due to longitudinal fibre breakage. In terms of failure mechanisms, damage initiation and progression up to final failure in on-axis 3D woven composites has been reported in [16,28,31,32]. The damage initiation and progression were found to be similar for orthogonal, layer-to-layer and angle interlock architectures. The damage typically starts at the interlacement points between z-binder and warp (or weft) yarns where the local stress fields are amplified. Following the stress localisation at the interlacement points, transverse cracks within the yarns, perpendicular to the loading direction, grow instantaneously and multiply in number up to a saturation point. Then, the damage mechanism changes from

ACCEPTED MANUSCRIPT

transverse cracking to delamination (between warp and weft yarns and along the z-binder boundary), and this transition happens at the last stages of loading prior to fibre tow breakage.

Since the study of damage initiation and progression in off-axis 3D woven composite is very limited, here an interrupted test (at several load levels) was performed on the three architectures, and the underlying damage mechanisms were observed by X-ray machine (X-Tex XTH 225 cone-beam tomograph). The scanning spatial resolution was approximately 16 μm; and a diodomethane dye-penetrant from (Sigma Aldrich) was applied on the surface of specimens for one hour prior to scanning. Three stress levels (Points B, C, D) from the off-axis stress-strain curve of 3D woven composites were selected (see Fig. 9). The region of interest (ROI) for this observation is the centre of the specimen. Point A denotes zero stress where non-damage specimen was captured by X-ray as a reference. The strain level of the "knee point" in the off-axis tensile curves (and the corresponding tensile stress) of ORT, LTL and AI are given in Table 6. Point B was selected at the linear elastic segment (approximately 60 MPa) in order to characterise the damage initiation before the "knee point". Point C was around 110 MPa, which is a point after the knee point where damage progression was investigated. Point D was selected just before the specimen failure (around 95% of UTS), where the damage prior to failure was studied. The stress level for Point D was actually different for three architectures due to different UTS: the stress level is 210 MPa, 120 MPa and 170 MPa for ORT, LTL and AI specimens, respectively. X-ray images were captured with X-ray setting of 35 kV and 310 μA. To aid the damage analysis using X-ray, nomenclature of damage types is given in Table 7.

At Point A, no damage due to manufacturing is observed by X-ray. After the specimen was loaded to 60 MPa, the first damage characteristic at Point B observed in all architectures is free-edge matrix cracking (F-type). Damage at Point B is caused by the interlaminar stresses between layers as reported in [33–35]. Increasing the applied stress, F-type cracks propagate towards the centre of the specimens. Reaching Point C, three damage types are identified. ORT and AI specimens exhibited binder-induced damage (Z-type) at the interlacement points between the in-plane yarns and the binding yarns. Transverse

ACCEPTED MANUSCRIPT

cracking (T-type) within yarns starts to multiply in number associated with inter-yarn matrix delamination (D-type). The (D-type) damage is driven by the in-plane yarns realignment and rotation towards the loading axis (see Section 4.5). In case of LTL specimen, accumulation of the (D-type) cracks is more severe as it has the least strength (~130 MPa) while no Z-type damage can be observed. Up to this stress level, there is no significant difference in the damage mechanisms between the three architectures. At Point D (~95% UTS), the damage accumulation and evolution changed dramatically. In ORT specimen, D-type cracks are arrested by the z-binder yarns while (T-type) cracks multiple in number. In ORT specimen, damage is uniformly distributed over the ROI. In LTL and AI specimen, a different type of damage takes place, namely the slippage between in-plane yarns (S-type) that leads to an extensive localised damage which directly results in the reduction of specimen's width.

The next step is to investigate whether the damage is homogenously distributed over the full gauge length of the specimen or not. So, three ROIs (top, centre, and bottom) of the specimen were scanned by X-ray, and "stitched" together as shown in Fig. 10. Three scans at different regions were carried out to maintain good image resolution. The horizontal lines seen in the X-ray images are the marking lines made to ensure correct transition for image stitching. Table 8 summarises the sequence of damage in the off-axis loaded specimens made by this X-ray analysis.

At 210 MPa (95% of UTS), as ORT specimen has smaller unit cell size (higher z-binder density) than LTL and AI, this enables stress redistribution over a longer span of the specimen, and prevents the slippage between in-plane yarns. Thus, the damage in ORT is seen to be uniformly distributed all over the gauge length of the specimen. On the contrary, both LTL and AI specimens exhibited localised damage due to S-type damage and extensive inter-yarn delamination. This is actually reflected in the global failure as shown in (Fig. 11). ORT specimens broke into two separate parts (Fig. 11a) with angled fracture where breakage of the z-binders is evident around the fracture area. Failure of LTL and AI specimens shown in Figs. 11b and c, respectively, occurred in localised region that is characterised by angled fracture. No apparent ply separation was found in LTL and AI specimen as the z-binder yarns prevented the separation between warp and weft layers.

ACCEPTED MANUSCRIPT

To further understand the underlying damage mechanisms, the failed specimens were X-ray scanned at different locations, i.e. close to the fracture region and away from it. After reconstructing the 3D scanned volumes, cross-sectional slices parallel to the binder plane "rotated 45o from the loading direction" are extracted (see Fig. 12). The three different locations are chosen in a systematic manner to show the damage in regions where there is no binder (Fig. 12a), with binder (Fig. 12b) and close to the fracture region (Fig. 12c). ORT scans show extensive transverse cracking homogenously distributed across the width of the specimen (Fig. 12a). In regions where the binding yarns exist (Fig. 12b), no inter-yarn delamination is observed as opposed to regions where there are no binding yarns (Fig. 12a). In addition, localised damage (Fig. 12b) occurs due to binder interlacing with weft/ warp yarns. Final failure happens when the binding yarns fracture (Fig. 12c) followed by extensive delamination. For LTL architecture, transverse cracking and delamination, between warp and weft layers (Fig. 12a), spans the whole width of the specimen. In regions with binding yarns, delamination is guided by their path (Fig. 12b). Close to the fracture region, the slippage (Fig. 12c) between planes and ply separations due to binders' breakage characterises the damage mechanism resulting into final failure. In case of AI architecture, multiple transverse cracking (Fig. 12a, b) is observed in the in-plane yarns "warp/ weft" with inter-yarn delamination (Fig. 12a-c). Localised induced damage (Fig. 12b) due to binder interlacement is clear in the form of matrix cracking. When binding yarns break, ply separation, between warp and weft planes, is observed (Fig. 12c) leading to final failure of the specimen.

4.5 Effect of z-binder on energy absorption

The energy absorbed per unit volume up to fracture (in MJ/m^3) is calculated as the area under the stress-strain curve. The energy absorption of 3D woven composites with different z-binder architectures is shown in Fig. 13. It is obvious that the specimens loaded in off-axis direction demonstrate greater energy absorption in comparison with their on-axis counterparts. More importantly, the z-binder architecture has a significant effect on the energy absorption of the off-axis loaded specimens. Under off-axis loading, ORT architecture absorbs energy almost three times higher than other 3D architectures. Furthermore, ORT specimens loaded in off-axis direction absorbs energy five times higher than that loaded in on-axis direction. This suggest the following: (i) based on energy

ACCEPTED MANUSCRIPT

absorption criterion, all 3D woven composites perform better under off-axis rather than on-axis loading; (ii) among all 3D woven composites investigated here, ORT performs the best in terms of energy absorption under off-axis loading. These findings can be used for the analysis of composite structures which may employ 3D woven composites for better response under multi-axial loading and impact resistance, where energy absorption is of prime interest.

When 3D woven composite are subjected to off-axis loading, the warp and weft yarns that are biased with certain angle tend to reorient towards the principal loading axis. During the reorientation process, the so-called "scissoring effect" takes place between the warp, weft and binder yarns. This reorientation process allows further strain to be borne by the composite laminate and consequently energy absorption. Table 9 shows the rotation angles of 3D woven composites measured experimentally 95% UTS of the different specimens.

ORT specimens exhibit the largest rotation angle as compared to other specimens indicating that orthogonal z-binder coupled with small unit cells provides the best interlocking mechanism for in-plane yarns. The interlocking mechanism, with high fibre rotation angle at failure as exemplified by ORT 3D woven composites, improves their shear performance (failure strain, energy absorption) compared to other woven architectures.

5 Concluding remarks

Different architectures of 3D woven composites (orthogonal, ORT; layer-to-layer, LTL; angle interlock, AI) were characterised in terms of on-axis and off-axis mechanical properties and the influence of z-binder. Several remarks can be made from present investigation. The z-binder increases void content in 3D woven composites since the amount of resin flowing between warp and weft tows is partly inhibited by the binders; in this case, orthogonal architecture induces the highest amount of void in comparison to other architectures. Regardless of the weaving architecture type, the stiffness and tensile strength of 3D woven composites under on-axis loading mainly depends on the directional fibre volume fraction of warp and weft yarns. Among all textile architectures, 3D orthogonal woven composites exhibit the best performance (highest failure strength and failure strain)

ACCEPTED MANUSCRIPT

under off-axis loading due to interlocking mechanism provided by z-binder. This interlocking mechanism increases the rotation angle of warp and weft yarns, and thus the ability of the yarns to bear extensive off-axis strain. Moreover, as the ORT specimen has smaller unit cell size and higher z-binder density, this enables the stress redistribution over a longer span of the specimen, and prevents the slippage between in-plane yarns. So, the damage is uniformly distributed all over the gauge length of the specimen. The 3D orthogonal woven composites exhibit the highest energy absorption among other architectures during off-axis loading, which may pave the way for their use in composite structures designed with energy criterion as well as impact performance.

6 Acknowledgments

Authors would like to acknowledge the financial support from University of Manchester (UoM) and from Baseline Research Funds from King Abdullah University of Science and Technology (KAUST). We also acknowledge the technical support from the Northwest Composites Certification and Evaluation Facility (NCCEF). We would also like to thank Dr. Adam Joesbury from NCCEF for his helpful technical discussions.

7 References

[1] Stig F. 3D-woven Reinforcement in Composites. 2012.

[2] Hao A, Sun B, Qiu Y, Gu B. Dynamic properties of 3-D orthogonal woven composite T-beam under transverse impact. Compos Part A Appl Sci Manuf 2008;39:1073–82. doi:10.1016/j.compositesa.2008.04.012.

[3] Ji C, Sun B, Qiu Y, Gu B. Impact damage of 3D orthogonal woven composite circular plates. Appl Compos Mater 2007;14:343–62. doi:10.1007/s10443-008-9050-x.

[4] Luo Y, Lv L, Sun B, Qiu Y, Gu B. Transverse impact behavior and energy absorption of three-dimensional orthogonal hybrid woven composites. Compos Struct 2007;81:202–9. doi:10.1016/j.compstruct.2006.08.011.

[5] Seltzer R, González C, Muñoz R, LLorca J, Blanco-Varela T. X-ray microtomography analysis of the damage micromechanisms in 3D woven

ACCEPTED MANUSCRIPT

composites under low-velocity impact. Compos Part A Appl Sci Manuf 2013;45:49–60. doi:10.1016/j.compositesa.2012.09.017.

[6] Gerlach R, Siviour CR, Wiegand J, Petrinic N. In-plane and through-thickness properties, failure modes, damage and delamination in 3D woven carbon fibre composites subjected to impact loading. Compos Sci Technol 2012;72:397–411. doi:10.1016/j.compscitech.2011.11.032.

[7] L. Tong, A.P. Mouritz MB. Chapter 2 Manufacture of 3D Fibre Preforms. 3D Fibre Reinf. Polym. Compos., 2009.

[8] Stig F, Hallström S. Influence of crimp on 3D-woven fibre reinforced composites. Compos Struct 2013;95:114–22. doi:10.1016/j.compstruct.2012.07.022.

[9] Stig F, Hallström S. Assessment of the mechanical properties of a new 3D woven fibre composite material. Compos Sci Technol 2009;69:1686–92. doi:10.1016/j.compscitech.2008.04.047.

[10] L. Tong, A.P. Mouritz MB. Chapter 5 3D Woven Composites. 3D Fibre Reinf. Polym. Compos., 2009.

[11] Dai S, Cunningham PR, Marshall S, Silva C. Influence of fibre architecture on the tensile, compressive and flexural behaviour of 3D woven composites. Compos Part A Appl Sci Manuf 2015;69:195–207. doi:10.1016/j.compositesa.2014.11.012.

[12] Ansar M, Xinwei W, Chouwei Z. Modeling strategies of 3D woven composites: A review. Compos Struct 2011;93:1947–63. doi:10.1016/j.compstruct.2011.03.010.

[13] Behera BK, Dash BP. Mechanical behavior of 3D woven composites. Mater Des 2015;67:261–71. doi:10.1016/j.matdes.2014.11.020.

[14] Cox BN, Dadkhah MS, Morris WL, Flintoff JG. Failure mechanisms of 3D woven composites in tension, compression, and bending. Acta Metall Mater 1994;42:3967–84. doi:10.1016/0956-7151(94)90174-0.

[15] Cox BN, Dadkhah MS, Morris WL. On the tensile failure of 3D woven composites. Compos Part A Appl Sci Manuf 1996;27:447–58. doi:10.1016/1359-835X(95)00053-5.

ACCEPTED MANUSCRIPT

[16] Lomov S V, Bogdanovich a E, Karahan M, Mungalov D, Verpoest I, Leuven KU. Mechanical Behaviour of Non-Crimp 3D Woven Carbon / Epoxy Composite Under in-Plane Tensile Loading. ICCM 18, 2011, p. 1–5.

[17] Leong KH, Lee B, Herszberg I, Bannister MK. Effect of binder path on the tensile properties and failure of multilayer woven CFRP composites. Compos Sci Technol 2000;60:149–56. doi:10.1016/S0266-3538(99)00108-6.

[18] Quinn JP, McIlhagger a. T, McIlhagger R. Examination of the failure of 3D woven composites. Compos Part A Appl Sci Manuf 2008;39:273–83. doi:10.1016/j.compositesa.2007.10.012.

[19] Pochiraju K. Three-Dimensionally Woven and Braided Composites. II: An Experimental Characterization. Polym Compos 1999;20:733–47.

[20] Tan P, Tong L, Steven GP, Ishikawa T. Behavior of 3D orthogonal woven CFRP composites. Part I. Experimental investigation. Compos Part A Appl Sci Manuf 2000;31:259–71. doi:10.1016/S1359-835X(99)00070-6.

[21] Warren KC, Lopez-Anido R a., Goering J. Experimental investigation of three-dimensional woven composites. Compos Part A Appl Sci Manuf 2015;73:242–59. doi:10.1016/j.compositesa.2015.03.011.

[22] Visrolia a., Meo M. Multiscale damage modelling of 3D weave composite by asymptotic homogenisation. Compos Struct 2013;95:105–13. doi:10.1016/j.compstruct.2012.07.018.

[23] Vallons K, Duque I, Lomov SV, Verpoest I. Loading direction dependence of the tensile stiffness, strength and fatigue life of biaxial carbon/epoxy NCF composites. Compos Part A Appl Sci Manuf 2011;42:16–21. doi:10.1016/j.compositesa.2010.09.009.

[24] Ivanov DS, Lomov S V., Bogdanovich AE, Karahan M, Verpoest I. A comparative study of tensile properties of non-crimp 3D orthogonal weave and multi-layer plain weave E-glass composites. Part 2: Comprehensive experimental results. Compos Part A Appl Sci Manuf 2009;40:1144–57. doi:10.1016/j.compositesa.2009.04.032.

[25] Yudhanto A, Lubineau G, Ventura IA, Watanabe N, Iwahori Y, Hoshi H. Damage

ACCEPTED MANUSCRIPT

characteristics in 3D stitched composites with various stitch parameters under in-plane tension. Compos Part A Appl Sci Manuf 2015;71:17–31. doi:10.1016/j.compositesa.2014.12.012.

[26] Jia X, Xia Z, Gu B. Micro/meso-scale damage analysis of three-dimensional orthogonal woven composites based on sub-repeating unit cells. J Strain Anal Eng Des 2012;47:313–28. doi:10.1177/0309324712444671.

[27] Daggumati S, Van Paepegem W, Degrieck J, Praet T, Verhegghe B, Xu J, et al. Local strain in a 5-harness satin weave composite under static tension: Part II - Meso-FE analysis. Compos Sci Technol 2011;71:1217–24. doi:10.1016/j.compscitech.2011.03.020.

[28] Obert E, Daghia F, Ladevèze P, Ballere L. Micro and meso modeling of woven composites: Transverse cracking kinetics and homogenization. Compos Struct 2014;117:212–21. doi:10.1016/j.compstruct.2014.06.035.

[29] Blaysat B, Florentin E, Lubineau G, Moussawi A. A Dissipation Gap Method for full-field measurment-based identification of elasto-plastic material parameters. Proc 2011 Am Control Conf 2011:1885–91. doi:10.1002/nme.

[30] Fuller JD, Wisnom MR. Pseudo-ductility and damage Suppression in thin ply angle-ply carbon-epoxy laminates. Compos Part A Appl Sci Manuf 2013;69:64–71. doi:10.1016/j.compositesa.2014.11.004.

[31] Yu B, Bradley RS, Soutis C, Hogg PJ, Withers PJ. 2D and 3D imaging of fatigue failure mechanisms of 3D woven composites. Compos Part A Appl Sci Manuf 2015. doi:10.1016/j.compositesa.2015.06.013.

[32] Bogdanovich AE, Karahan M, Lomov S V., Verpoest I. Quasi-static tensile behavior and damage of carbon/epoxy composite reinforced with 3D non-crimp orthogonal woven fabric. Mech Mater 2013;62:14–31. doi:10.1016/j.mechmat.2013.03.005.

[33] Mittelstedt C, Becker W. Free-Edge Effects in Composite Laminates. Appl Mech Rev 2007;60:217. doi:10.1115/1.2777169.

[34] Mittelstedt C, Becker W. Interlaminar Stress Concentrations in Layered Structures: Part I - A Selective Literature Survey on the Free-Edge Effect since 1967. J Compos

ACCEPTED MANUSCRIPT

Mater 2004;38:1037–62. doi:10.1177/0021998304040566.

[35] Sun CT, Zhou SG. Failure of Quasi-Isotropic Composite Laminates with Free Edges. J Reinf Plast Compos 1988;7:515–57. doi:10.1177/073168448800700602.

ACCEPTED MANUSCRIPT

ACCEPTED MANUSCRIPT

List of Figures

ACCEPTED MANUSCRIPT

ACCEPTED MANUSCRIPT

List of Tables

ACCEPTED MANUSCRIPT

ACCEPTED MANUSCRIPT

Table 1. Specification of textile architecture of 3D woven composites

Parameter	ORT	LTL	AI
Warp fibre count	12k	12k	12k
Weft fibre count	12k	12k	12k
z-binder fibre count	6k	12k	6k
Ends/cm (warp)	31.52	17.73	31.52
Picks/cm (weft)	38	36	34
Binders/cm (z-binder)	3.94	17.73	3.94
Areal density (g/m^2)	3353	3260	3044

Table 2. Volume fraction of constituents (fibre, matrix, void) in 3D woven composites

Constituent	3D composite		
	ORT	LTL	AI
Fibre (%)	51.35 ± 0.45	59.16 ± 0.24	55.4 ± 0.80
Matrix (%)	46.02 ± 0.43	39.21 ± 0.14	42.18 ± 0.97
Voids (%)	2.63 ± 0.02	1.63 ± 0.13	2.42 ± 0.19

Table 3. Directional fibre volume fraction in 3D woven composites

Direction of fibre tow	ORT	LTL	AI
Warp (%)	21.57	14.36	25.58
Weft (%)	26.00	29.15	27.59
z-binder (%)	3.77	15.65	2.22

Table 4. Young's modulus, tensile strength and failure strain of 3D composites in warp and weft directions

Textile architecture	Young's modulus (GPa)		Tensile strength (MPa)		Failure strain (%)	
	Warp (0°)	Weft (90°)	Warp (0°)	Weft (90°)	Warp (0°)	Weft (90°)
ORT	56.6 ± 0.39	70.0 ± 1.86	711 ± 17.39	862 ± 23.07	1.20 ± 0.02	1.25 ± 0.03
LTL	53.9 ± 0.46	76.6 ± 0.84	681 ± 21.82	1029 ± 29.82	1.37 ± 0.04	1.34 ± 0.05
AI	71.0 ± 1.92	69.9 ± 1.42	913 ± 40.26	924 ± 31.68	1.28 ± 0.08	1.28 ± 0.09

ACCEPTED MANUSCRIPT

Table 5. Off-axis tensile modulus, strength and failure strain of 3D woven composites

Textile architecture	Tensile Modulus (GPa)	Tensile strength (MPa)	Failure strain (%)
ORT	7.93 ± 0.25	226.33 ± 11.04	24.20 ± 1.22
LTL	9.93 ± 0.37	132.02 ± 3.71	11.27 ± 0.33
AI	8.82 ± 0.28	172.76 ± 0.55	13.29 ± 0.48

Table 6 Strain and stress levels at the "knee point" for off-axis tensile test

Textile architecture	Axial strain (%)	Tensile stress (MPa)
ORT	1.84 ± 0.19	88.91 ± 2.80
LTL	1.45 ± 0.03	90.88 ± 2.58
AI	1.71 ± 0.16	94.70 ± 0.86

Table 7. Nomenclature of damage types

Code	**Damage type**
F	Free edge matrix crack between yarns
Z	Z-binder induced damage
T	Transverse crack within yarns
D	Inter-yarn matrix delamination
S	Slippage between in-plane tows “warp/weft”

Table 8. Sequence of damage events during tensile loading of off-axis 3D woven composites

Point	**Applied stress (MPa)**	**ORT**	**LTL**	**AI**
A	0	--	--	--
B	60	F	F	F
C	110	F,T,Z	F,T,D	F,T,Z
D	95% UTS (210, 120,170)	F,T,D,Z	F,T,D,S	F,T,D ,Z,S

Table 9. Experimental rotation angles for off-axis specimens at 95% UTS

Parameter	ORT	LTL	AI
Exp. Rotation angle (deg)	12.07 ± 0.12	7.93 ± 0.49	5.43 ± 0.73

ACCEPTED MANUSCRIPT

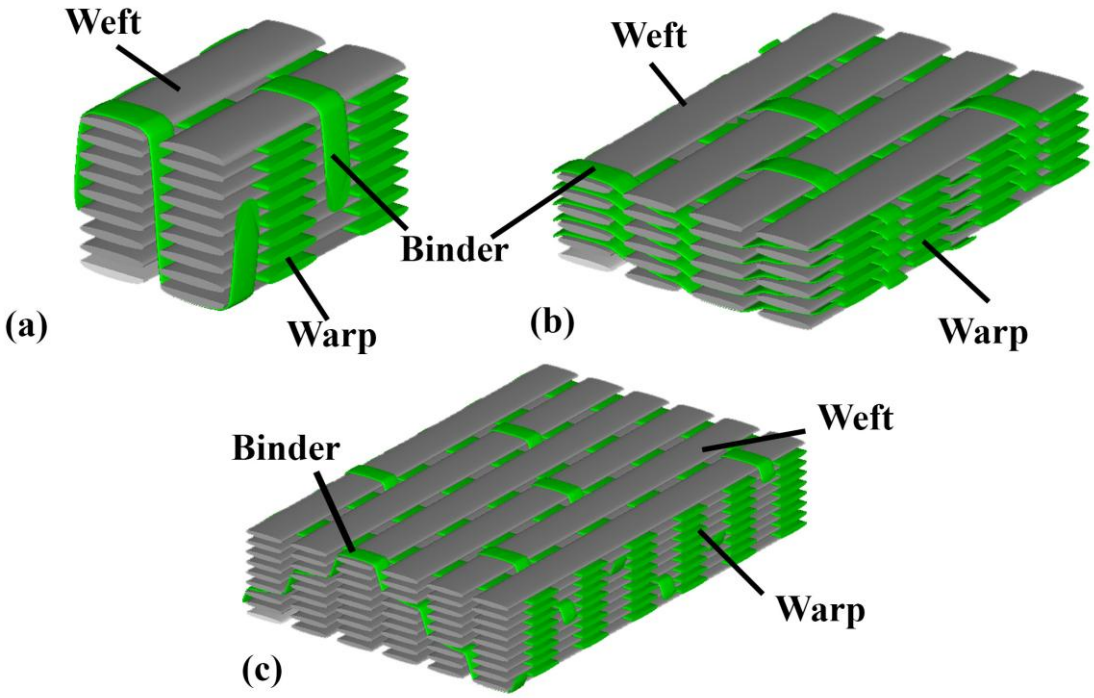

ACCEPTED

ACCEPTED MANUSCRIPT

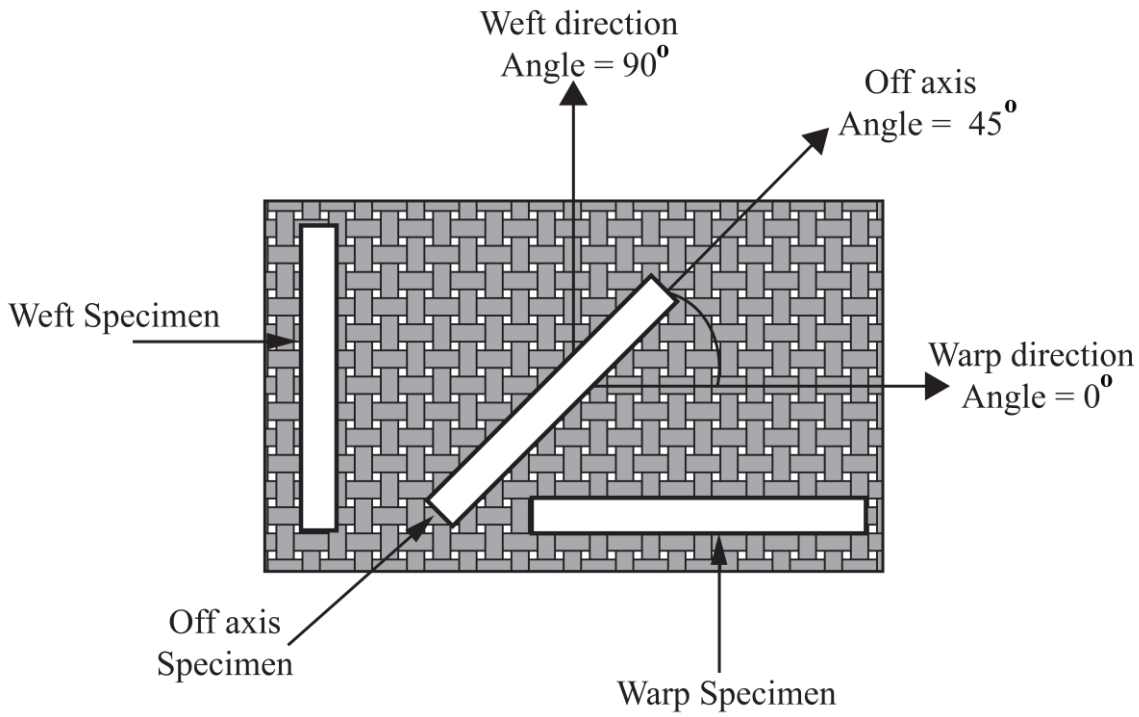

ACCEPTED MANUSCRIPT

ACCEPTED MANUSCRIPT

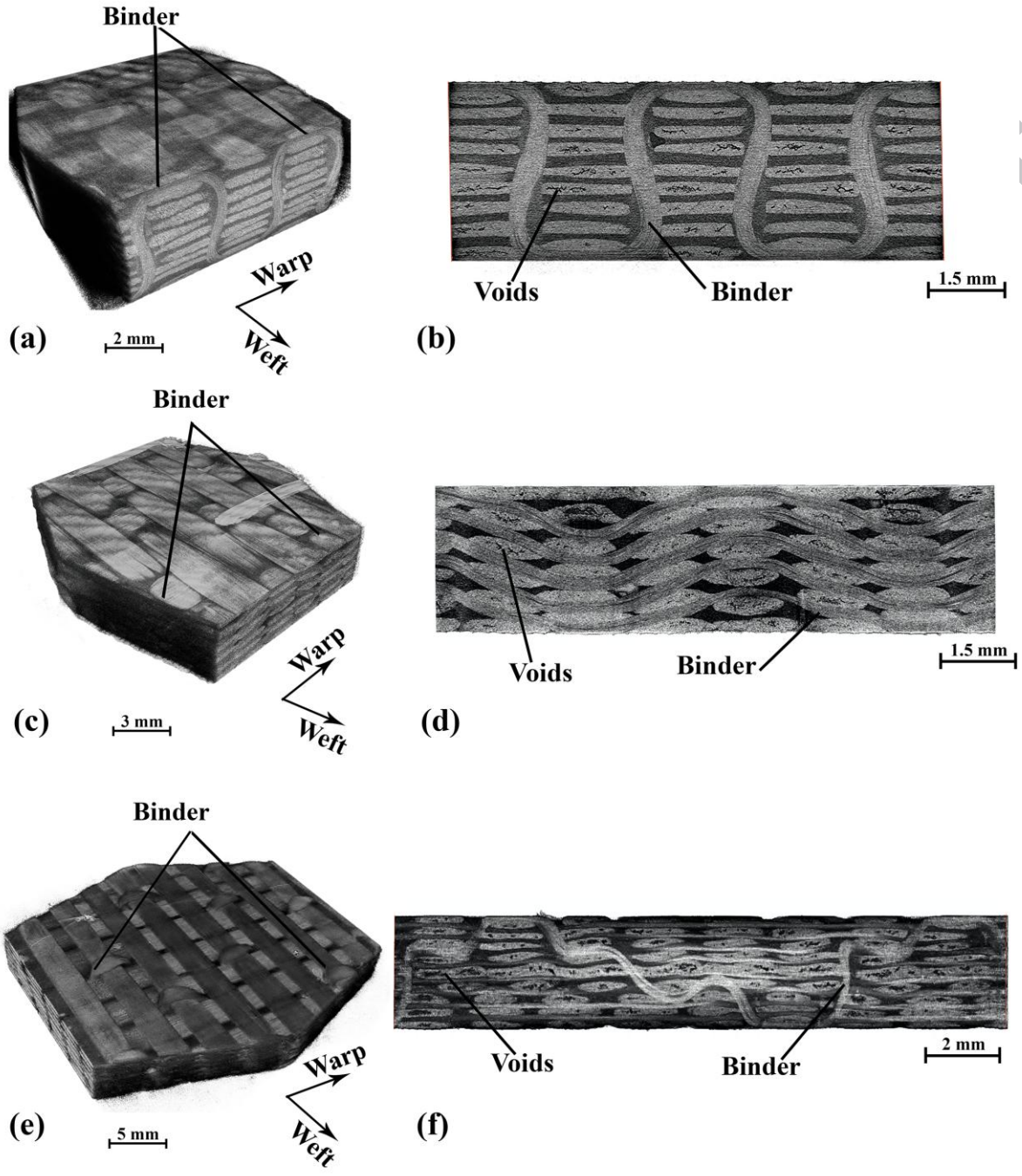

ACCEPTED MANUSCRIPT

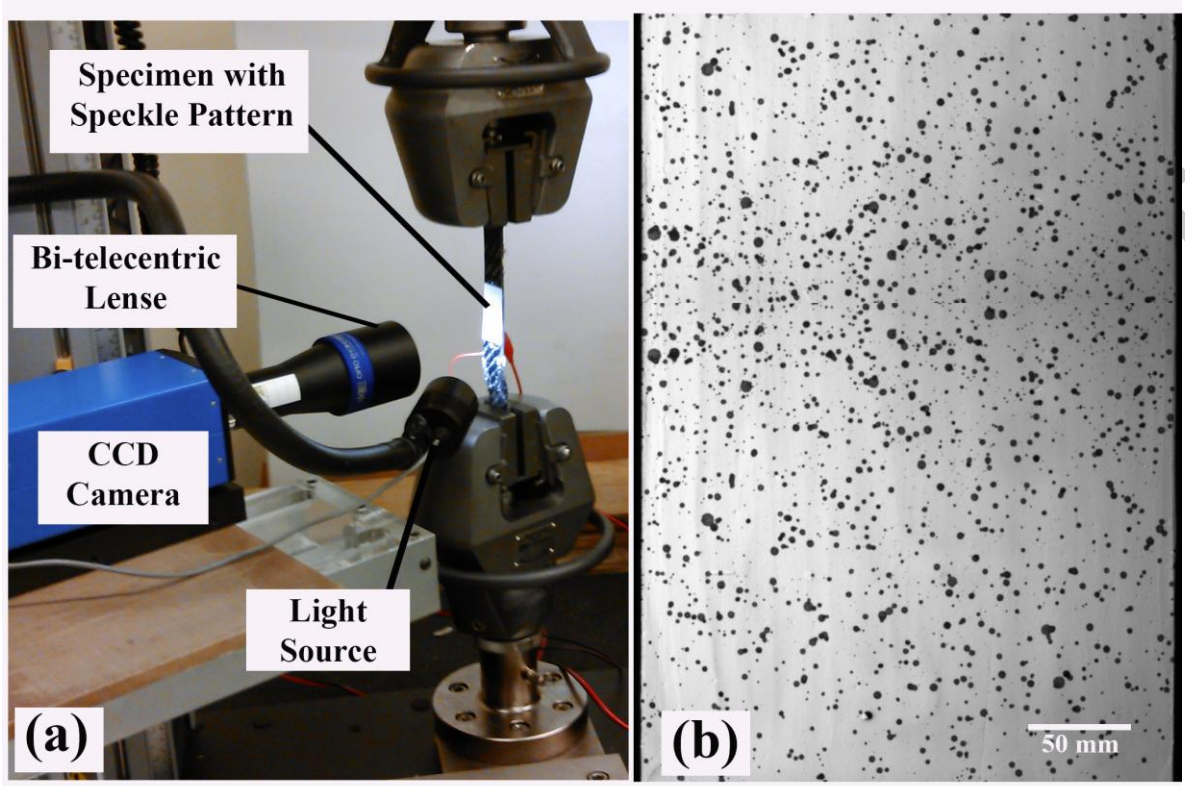

ACCEPTED MANUSCRIPT

ACCEPTED MANUSCRIPT

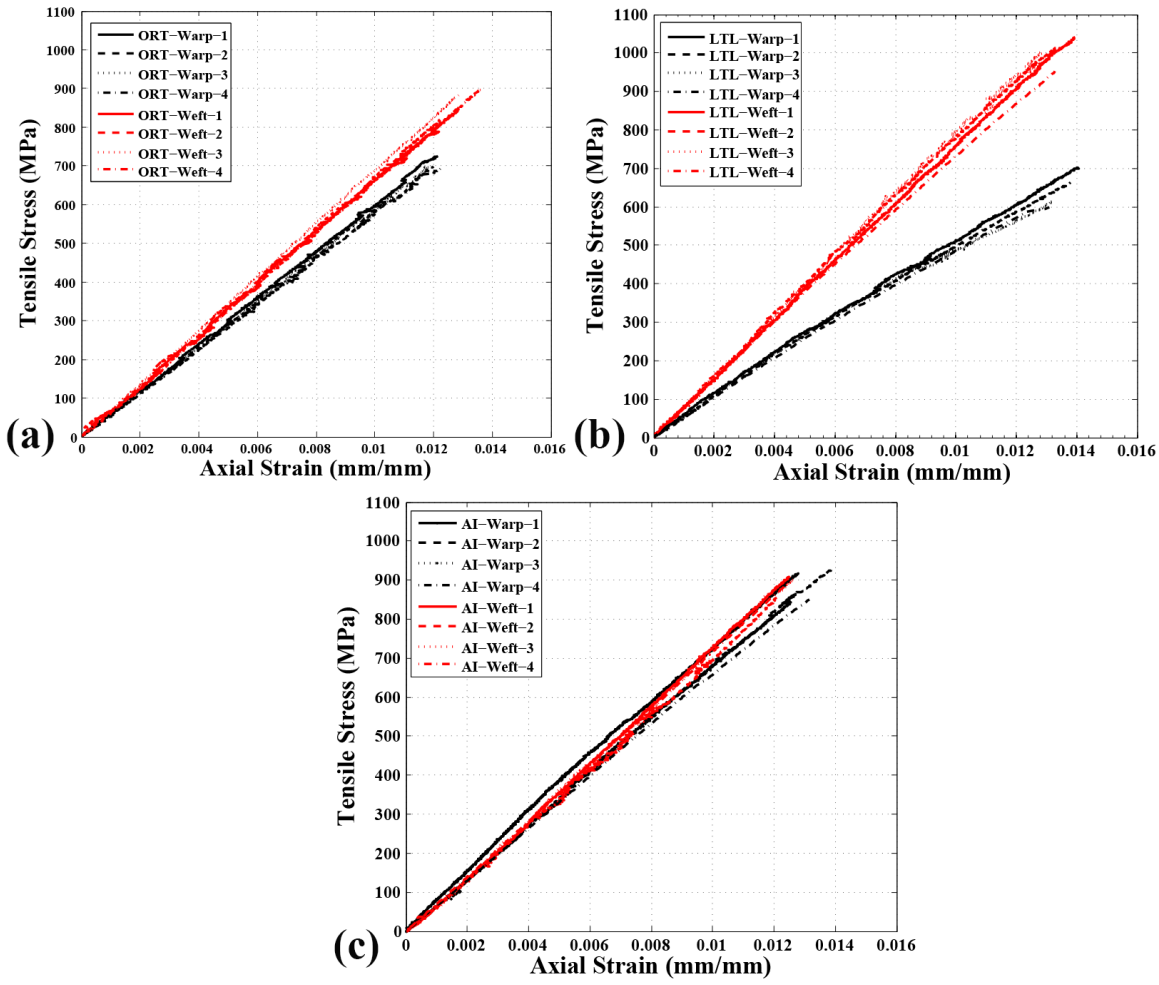

ACCEPTED

ACCEPTED MANUSCRIPT

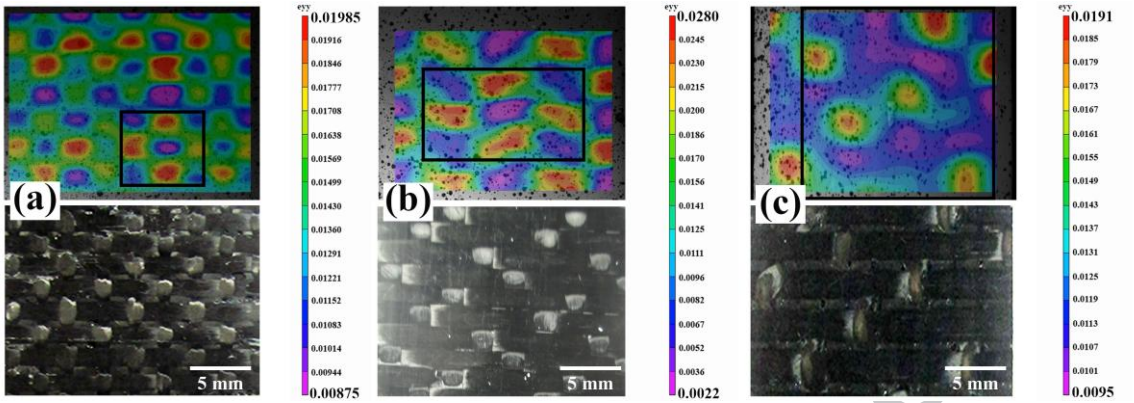

ACCEPTED MANUSCRIPT

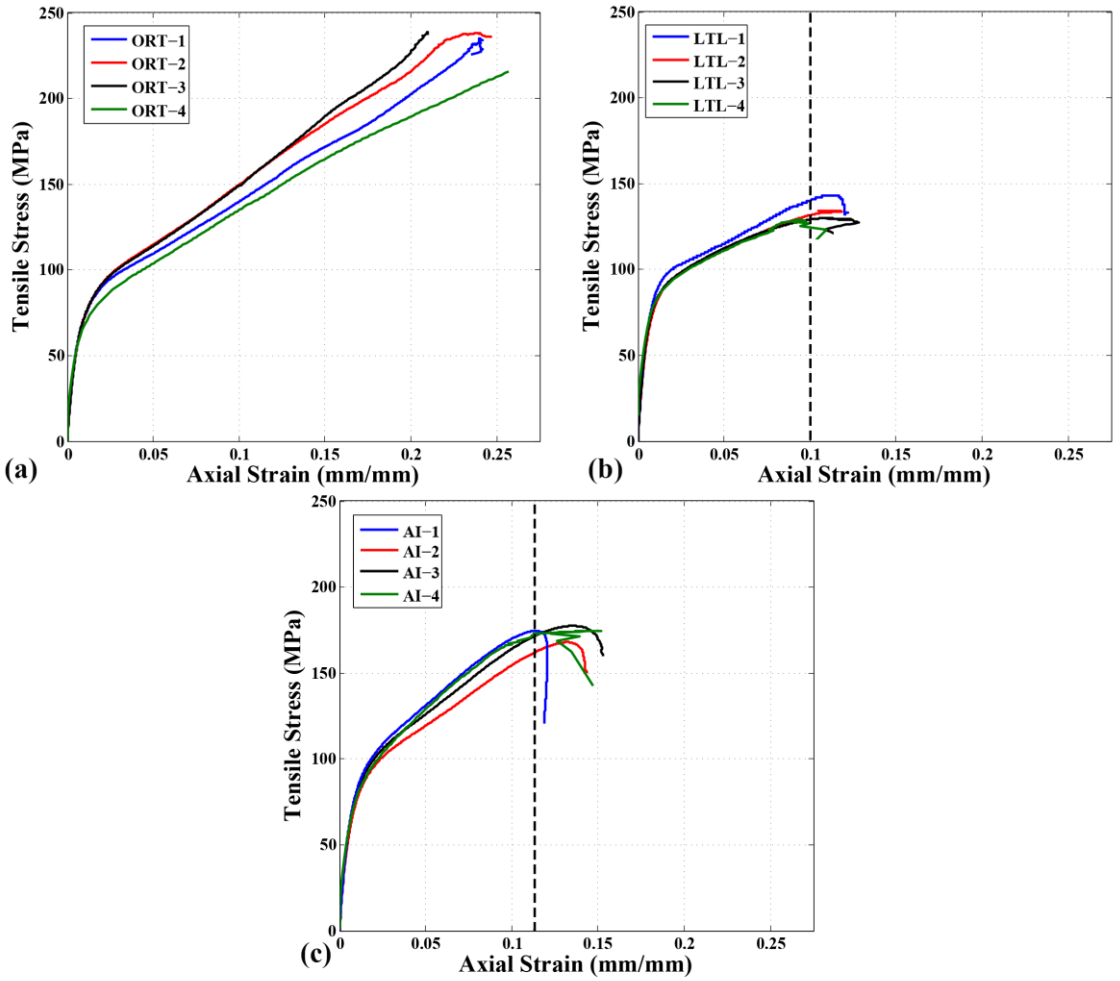

ACCEPTED MANUSCRIPT

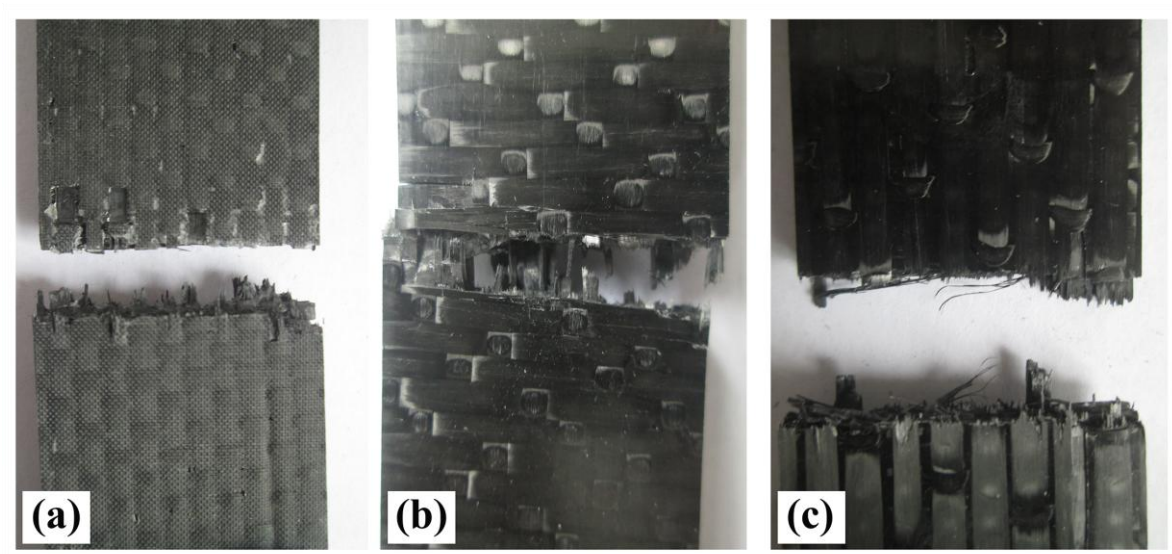

ACCEPTED MANUSCRIPT

ACCEPTED MANUSCRIPT

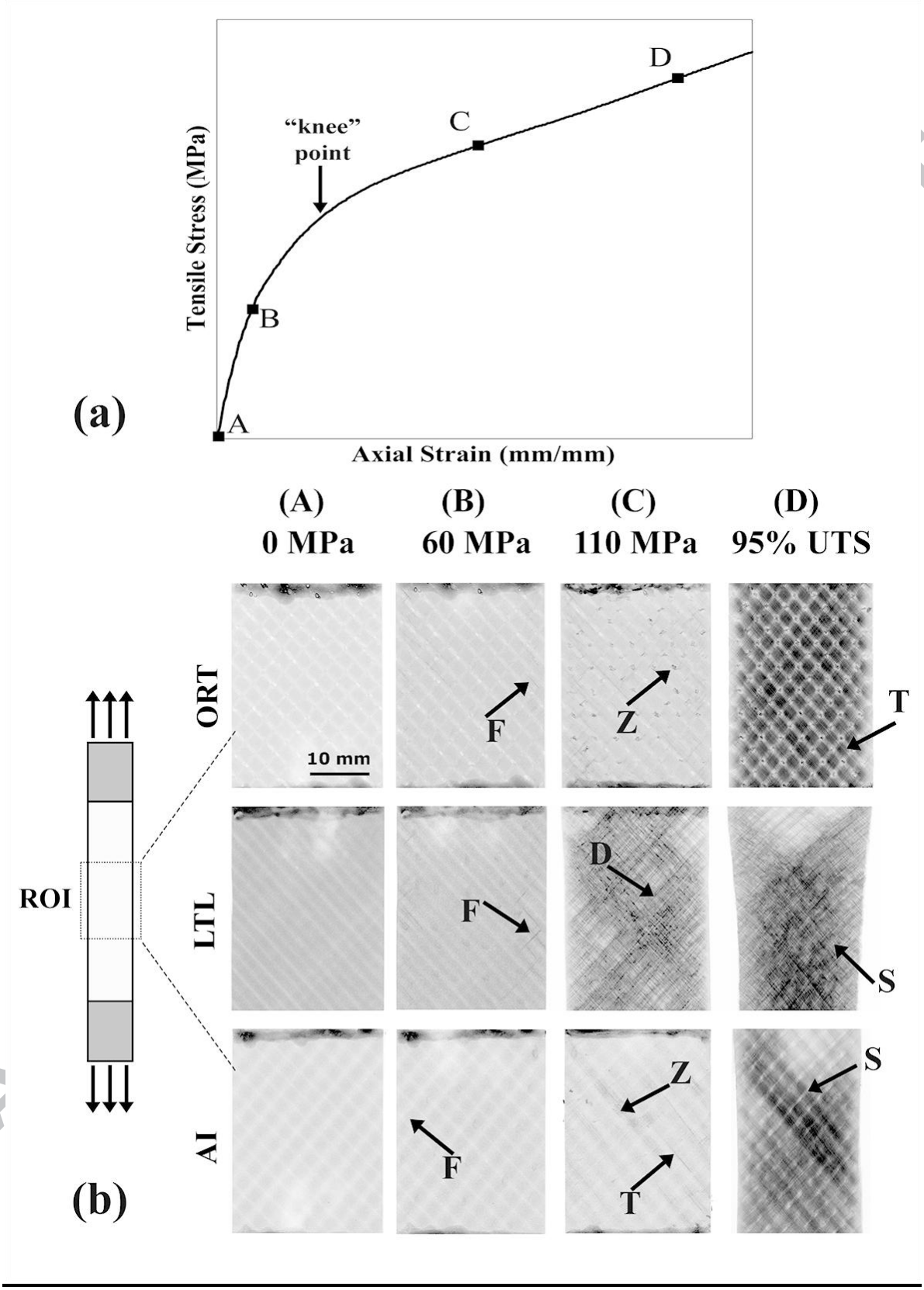

ACCEPTED MANUSCRIPT

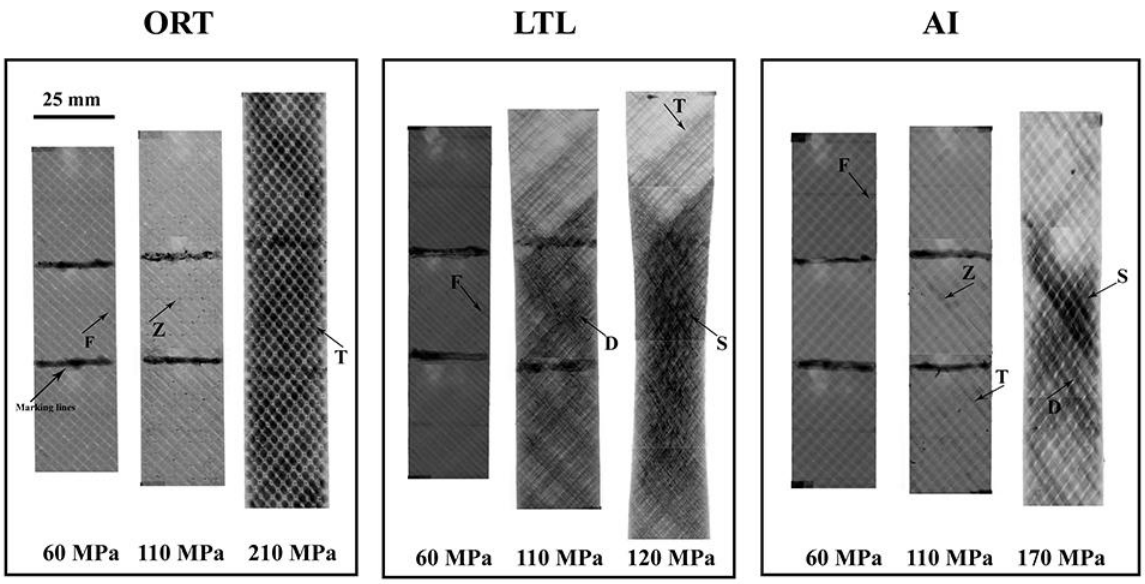

ACCEPTED MANUSCRIPT

ACCEPTED MANUSCRIPT

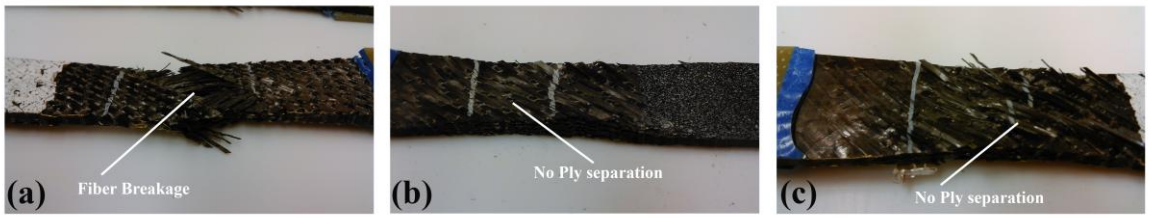

ACCEPTED MANUSCRIPT

ACCEPTED MANUSCRIPT

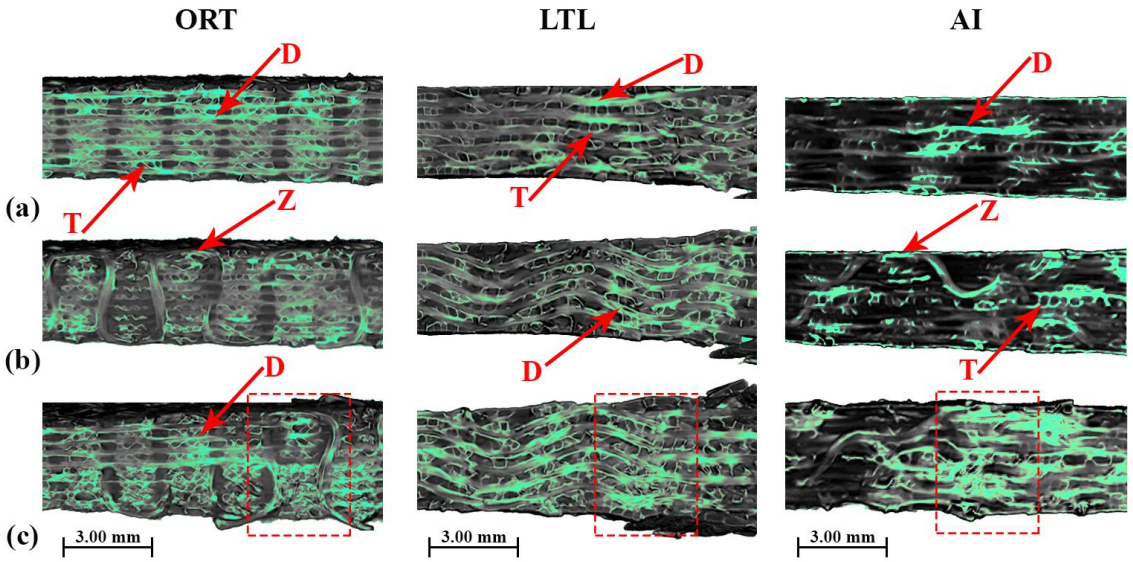

ACCEPTED MANUSCRIPT

ACCEPTED MANUSCRIPT

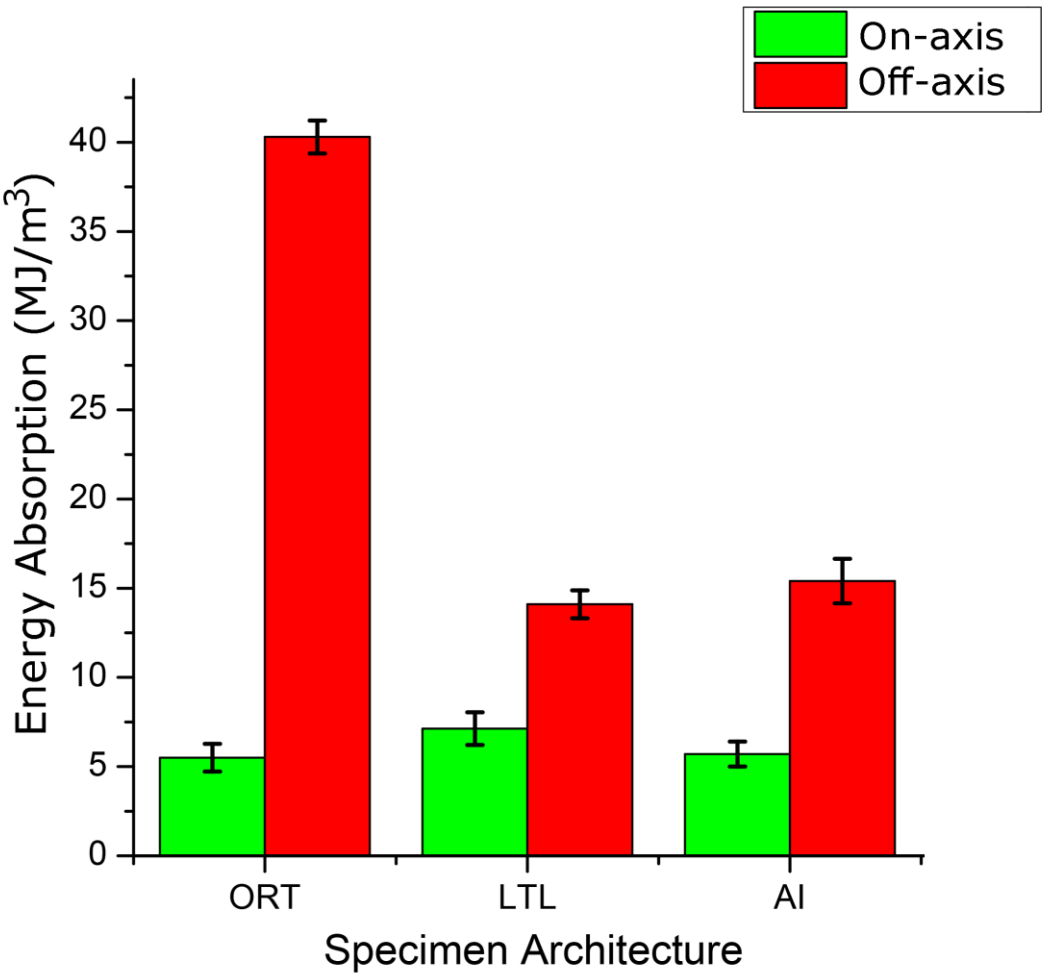

ACCEPTED